Complexes of HNO_3 and NO_3^- with NO_2 and N_2O_4, and their potential role in atmospheric HONO formation†

Michael A. Kamboures,[a] Jonathan D. Raff,[a] Yifat Miller,[b] Leon F. Phillips,[c] Barbara J. Finlayson-Pitts[a] and R. Benny Gerber*[ab]

Received 31st March 2008, Accepted 21st July 2008
First published as an Advance Article on the web 11th August 2008
DOI: 10.1039/b805330h

Calculations were performed to determine the structures, energetics, and spectroscopy of the atmospherically relevant complexes $(HNO_3)\cdot(NO_2)$, $(HNO_3)\cdot(N_2O_4)$, $(NO_3^-)\cdot(NO_2)$, and $(NO_3^-)\cdot(N_2O_4)$. The binding energies indicate that three of the four complexes are quite stable, with the most stable $(NO_3^-)\cdot(N_2O_4)$ possessing binding energy of almost -14 kcal mol^{-1}. Vibrational frequencies were calculated for use in detecting the complexes by infrared and Raman spectroscopy. An ATR-FTIR experiment showed features at 1632 and 1602 cm^{-1} that are attributed to NO_2 complexed to NO_3^- and HNO_3, respectively. The electronic states of $(HNO_3)\cdot(N_2O_4)$ and $(NO_3^-)\cdot(N_2O_4)$ were investigated using an excited state method and it was determined that both complexes possess one low-lying excited state that is accessible through absorption of visible radiation. Evidence for the existence of $(NO_3^-)\cdot(N_2O_4)$ was obtained from UV/vis absorption spectra of N_2O_4 in concentrated HNO_3, which show a band at 320 nm that is blue shifted by 20 nm relative to what is observed for N_2O_4 dissolved in organic solvents. Finally, hydrogen transfer reactions within the $(HNO_3)\cdot(NO_2)$ and $(HNO_3)\cdot(N_2O_4)$ complexes leading to the formation of HONO, were investigated. In both systems the calculated potential profiles rule out a thermal mechanism, but indicate the reaction could take place following the absorption of visible radiation. We propose that these complexes are potentially important in the thermal and photochemical production of HONO observed in previous laboratory and field studies.

Introduction

Reactions in and on thin water films on surfaces are of intrinsic chemical interest because their kinetics and mechanisms may be quite different from those in the bulk aqueous or gas phase. For example, the hydrolysis of NO_2 is very slow in both phases, yet it is known to occur at a measurable rate in thin water films on surfaces:[1]

$$2NO_2 + H_2O \rightarrow HONO + HNO_3 \qquad (1)$$

This reaction is potentially important in the lower atmosphere as a source of gaseous HONO, which has been shown by a number of studies to be a major photolytic source of the highly reactive OH free radical in continental regions:[1–5]

$$HONO + h\nu\ (\lambda < 400\ nm) \rightarrow OH + NO \qquad (2)$$

However, despite the importance of reaction (1), its mechanism is not well understood. In addition, both field[3,4,6–8] and laboratory studies[9–14] suggest that there is also a photochemically driven source of HONO in that system. While a photoreduction of NO_2 involving organics such as phenols or humic acid has been suggested,[12–14] this would not explain the production of HONO when a glass manifold exposed to HNO_3 was irradiated in the absence of organics.[10,15] In addition, organics are not required for photochemical HONO production in environmental chambers.[9,11,16–19]

While many of these studies suggest that HNO_3 and/or NO_3^- on surfaces are involved in the photochemistry, neither of these alone can explain the observations. HNO_3 has only a weak absorption tail in the actinic region above 290 nm that reaches Earth's surface,[1] and this generates NO_2 whose secondary thermal reactions to generate HONO are relatively slow. Although it had usually been assumed that HNO_3 formed during the NO_2 heterogeneous hydrolysis (reaction (1)) would dissociate to $H^+ + NO_3^-$, laboratory studies[20–22] show this is not entirely the case. In fact, at 50% relative humidity, almost half of the surface-bound species is in the form of undissociated HNO_3 that is complexed to water or itself.[22] Donaldson and coworkers[23] showed that hydrates of HNO_3 have electronic states that are nearly identical to those of isolated HNO_3, so that binding to water does not change the spectroscopy. Nitrate ions have a $n \rightarrow \pi^*$ transition that peaks at 310 nm, but this is also weak and decreases rapidly to negligible values at 340 nm.[24,25] In experiments performed in an environmental chamber (SAPHIR),[26] significant HONO production, up to 3 ppb h^{-1}, continued when a filter that only transmitted light above 370 nm

[a] *Department of Chemistry, University of California, Irvine, CA 92697, USA. E-mail: bgerber@uci.edu; Fax: +1 (1)9722651 3742; Tel: +1 (1)9722651 5732*
[b] *Department of Physical Chemistry and the Fritz Haber Research Center for Molecular Dynamics, Hebrew University, Jerusalem, 91904, Israel*
[c] *Department of Chemistry, University of Canterbury, Private Bag 4800, Christchurch, New Zealand*

† Electronic supplementary information (ESI) available: Vibrational frequencies, infrared intensities, and Raman intensities; additional configurations of $(HONO)\cdot(NO_3)$. See DOI: 10.1039/b805330h

was used, suggesting that the chromophore(s) responsible must absorb beyond 370 nm, and ruling out both HNO_3 and NO_3^- as the HONO precursor.

During the heterogeneous hydrolysis reaction (1), NO_2 and/or N_2O_4 must be taken up on the thin water film and it has been hypothesized[27–29] that a key step in the reaction is the isomerization of symmetric O_2NNO_2 to asymmetric $ONONO_2$. Both NO_2 and N_2O_4 absorb light to 400 nm and beyond.[1,30,31] Thus, one possible explanation for the field and laboratory observations may be the formation of complexes between NO_2 and/or N_2O_4 and HNO_3 or NO_3^- on surfaces. If the NO_2/N_2O_4 imbued the complexes with their chromophoric properties, photochemistry may occur that results in HONO formation. Such complexes may also play a previously unrecognized role in the thermal reaction (1).

Little is known about the structure, stability or spectroscopy of these potential complexes. Barnes *et al.*[32] reported the formation of a complex of NO_2 with HNO_3 in argon matrices at a temperature of 5 K, and a similar complex was tentatively identified in thin water films exposed to gas phase NO_2 at room temperature by Ramazan *et al.*[22] Indirect support for the involvement of NO_2/N_2O_4 comes from the SAPHIR chamber experiments in which the photochemical production rate of HONO could be parameterized by a term involving the photolysis rate of NO_2 in the chamber.[16] Li *et al.*[33] recently reported that electronically excited NO_2, generated by absorption beyond 420 nm, where dissociation to NO + $O(^3P)$ does not occur, reacts with water vapor to generate OH + HONO.

$$NO_2 + h\nu\ (\lambda > 420\ \text{nm}) \rightarrow NO_2^* \quad (3)$$

$$NO_2^* + H_2O \rightarrow OH + HONO \quad (4)$$

It seems unlikely that this is the source of HONO in the SAPHIR chamber experiments, as Rohrer *et al.*[26] ruled out photolysis primarily at $\lambda > 420$ nm based on the results of the cutoff filter experiments. Also, evidence suggests that reactions (3) and (4) may not be as strong a gas-phase HONO source as Li *et al.* proposed.[34,35]

There are also two earlier reports of enhanced HNO_3 photolysis in the presence of NO_2 at wavelengths of 366 and 265 nm[36,37] under anhydrous conditions, although traces of water may have been present. The observed loss of HNO_3 was eventually explained as being due to the heterogeneous reaction of NO with HNO_3 on the surfaces of the experimental apparatus.[38] However, under the high NO_2/N_2O_4 concentrations in those early experiments, it is possible that complexes between NO_2 and/or N_2O_4 and HNO_3 may have also been present and played a role in the observed enhancement of HNO_3 photolysis.

We have carried out theoretical and experimental studies of these complexes to assess their potential contribution to atmospheric heterogeneous chemistry. Specifically, we seek to: (1) identify the geometric structures and determine the stabilities of the complexes, $(HNO_3)\cdot(NO_2)$, $(NO_3^-)\cdot(NO_2)$, $(HNO_3)\cdot(N_2O_4)$, and $(NO_3^-)\cdot(N_2O_4)$; (2) calculate their vibrational frequencies, infrared intensities, and Raman activities, for use in detecting these complexes in laboratory experiments; (3) identify whether or not these complexes are chromophores using an excited state method; (4) examine the possibility that photochemically driven intramolecular hydrogen atom transfer reactions within the $(HNO_3)\cdot(NO_2)$ and $(HNO_3)\cdot(N_2O_4)$ complexes can lead to the formation of HONO; and (5) search for evidence of the complexes using infrared and UV/vis spectroscopy. While the results of the gas-phase calculations may not extrapolate quantitatively to conditions present on surfaces under atmospheric conditions, they can serve as a guide to determine if it is reasonable that such complexes play a role in atmospheric chemistry.

Methods

Computational details

The following electronic structure methods were used to determine the potential energies of chemical structures using the GAMESS suite of programs: (1) spin-restricted open-shell Hartree–Fock (ROHF)[39] (2) Becke-3-parameter exchange, Lee–Yang–Parr (B3LYP) correlation density functional theory,[40–42] and (3) spin-restricted open-shell Hartree–Fock with second order Møller–Plesset perturbation (ROMP2).[43] These methods were chosen for their ability to handle open-shell systems.

The GAMESS triple zeta valence basis set augmented with polarization functions on all atoms (TZP)[44] was used to model all molecular orbitals. This also accurately treated hydrogen bonding present in a number of the complexes investigated. The TZP basis set, along with MP2, was used recently by Miller *et al.*[45] to determine vibrational frequencies for similar H-bonded systems involving *cis*-HONO, *trans*-HONO, HNO_3, $(HNO_3)\cdot(H_2O)$ and HNO_4 that were in reasonable agreement with those obtained through experiments. Atomic charges were calculated using the Löwdin scheme in which the atomic orbitals and molecular orbital coefficients are converted to an orthogonal set generating electron populations that are less sensitive to basis set type.[46]

Electronic binding energies, D_0, were obtained for the complexes by taking the electronic potential energy of the optimized complex and subtracting from it the electronic potential energies of its subunits in their optimized isolated states. Zero point vibrational energy (ZPE) corrected binding energies, D_e, were obtained through a similar treatment. Corrections for basis set superposition errors (BSSE) were not made.

The electronic transitions of $(HNO_3)\cdot(N_2O_4)$, $(NO_3^-)\cdot(N_2O_4)$, and N_2O_4 were investigated using configuration interaction singles (CIS). All single substitutions of the ground state ROMP2/TZP spin orbitals by virtual orbitals were allowed. The wavefunction of the lowest energy excited electronic state of each chemical species was obtained. Vertical excitation energies to these states from their corresponding ground states, and the integrated intensities for these transitions (oscillator strengths) were computed. The λ_{max} absorption cross-section σ_A for transitions in the complexes were estimated from the ratios of the calculated integrated intensities, the absorption frequencies, and the experimental value of the absorption cross section for N_2O_4[31] with the assumption that the line shapes for the transitions in the complexes were identical to that of isolated N_2O_4.[47]

The CIS method generally overestimates excitation energies.[48–50] However, the method can be used to estimate shifts in the vertical excitation frequency of a chromophore due to changes in its chemical environment due to complexation and solvation.[23,49,51,52] In this study we calculated the absolute CIS vertical excitation energies of $(HNO_3)\cdot(N_2O_4)$ and $(NO_3^-)\cdot(N_2O_4)$ and corrected them by subtracting the difference between the calculated and experimental vertical excitation frequencies of isolated N_2O_4.[31,53]

Vibrational frequencies, infrared intensities, and Raman intensities were determined for all ROMP2-derived structures using the appropriate functions in GAMESS.[54–56] Vibrational frequencies calculated using the harmonic approximation may deviate from the experimental values. More accurate estimates of experimental vibrational frequencies of the complexes were obtained by applying the correction:

$$\nu_{exp}^{complex} = \nu_{calc}^{complex} + \Delta\nu_{subunit} \quad (5)$$

where $\nu_{exp}^{complex}$ is the predicted experimental frequency of a particular mode, $\nu_{calc}^{complex}$ is the uncorrected computed frequency, and $\Delta\nu_{subunit}$ is the difference (shift) between the computed and experimental frequency of the subunit taken from literature.

Infrared spectroscopy of surfaces exposed to HNO_3 and NO_x

IR spectra were collected using a Thermo Nicolet Avatar 370 Fourier transform infrared spectrometer equipped with an attenuated total reflection (ATR) probe (Axiom Analytical). The internal reflection element (IRE) installed at the end of the probe was either an AMTIR ($Ge_{33}As_{12}Se_{55}$) or silicon (Si) rod, 0.6 cm dia. × 4 cm long with 45° conical ends. The surface of the AMTIR rod was coated with a 20 nm thick (measured by ellipsometry) layer of SiO_x using plasma-enhanced chemical vapor deposition. The probe was cleaned between experiments by rinsing with water (Millipore, 18.2 MΩ cm) to remove adsorbed nitrate species. The spectrometer casing and interior of the ATR probe were purged with nitrogen to eliminate spectral interferences from water vapor and CO_2 in ambient air.

In a typical experiment, the ATR probe was inserted into a vacuum-tight borosilicate glass reaction chamber (1.75 L) and evacuated for 1–2 days at $\sim 10^{-4}$ Torr. Surfaces in the reaction chamber were conditioned by repeated exposure to ~20 Torr of NO_2–N_2O_4, followed by evacuation for 1 h at $\sim 10^{-4}$ Torr. The IRE was then exposed to anhydrous HNO_3 for 1 h before introducing a mixture of NO_2–N_2O_4 from the attached vacuum line. Single beam spectra were recorded under vacuum and then in the presence of mixtures of HNO_3, NO_2 and N_2O_4 at 295 ± 1 K. Infrared spectra were averages of 1000 scans recorded at a resolution of 2 cm^{-1}.

NO_2 was synthesized from the reaction of NO (Matheson, 99%) with excess oxygen (Oxygen Service Company, 99.993%), followed by trap-to-trap purification. Nitric oxide was purified by passing it through an acetone–dry ice bath trap at 195 K before use. Anhydrous HNO_3 was obtained from the vapor above a 1 : 2 v/v solution of HNO_3 (70 wt% HNO_3, 99.999 + %, Sigma-Aldrich) and H_2SO_4 (>95 wt%, Fluka).

Ultraviolet/visible spectroscopy of N_2O_4 solutions

Solutions of N_2O_4 in HNO_3 were prepared by trapping NO_2 (1% w/w) in a Schlenk flask containing concentrated HNO_3 under vacuum at 78 K, followed by warming to room temperature. The UV/vis absorption spectra of solutions of HNO_3–N_2O_4 and N_2O_4-free concentrated HNO_3 were obtained by adding a drop of either solution between two quartz microscope slides placed into a light path of the spectrophotometer. The solution of N_2O_4 in acetonitrile was prepared by adding tetrabutylammonium nitrate to excess nitrosonium tetrafluoroborate ($NOBF_4$) dissolved in anhydrous acetonitrile, in a glove bag under an atmosphere of dry N_2. Spectra of this solution were obtained in a quartz cell with a 0.1 mm pathlength.

All spectra were obtained at room temperature using an Ocean Optics HR4000 spectrophotometer. $NOBF_4$ (95%), tetrabutylammonium nitrate (97%), and anhydrous acetonitrile (99.8%) were from Sigma-Aldrich and used without further purification.

Results and discussion

NO_x complexes: structures and stabilities

Minimum energy structures of the binary complexes, $(HNO_3)\cdot(NO_2)$, $(HNO_3)\cdot(N_2O_4)$, $(NO_3^-)\cdot(NO_2)$ and $(NO_3^-)\cdot(N_2O_4)$ were located using ROHF, ROMP2, and B3LYP. Each method located one minimum for each complex. The binding energies for the four binary chemical complexes with and without zero-point energy (ZPE) corrections are shown in Table 1. Results indicate that the two complexes containing N_2O_4 possess substantially larger binding energies than the two complexes containing NO_2. In addition, the two complexes which contain NO_3^- have significantly greater binding energies than the two complexes that contain HNO_3. The structures and the stabilities for each of the four complexes are discussed below. It should be noted that the calculations presented here are all for the gas phase species. The substrate may have some impact on the calculated energetics of the complexes and the subunits, but this cannot be taken into account until there are data available on the nature of the interactions with the surface.

$(HNO_3)\cdot(NO_2)$

The ROMP2 optimized minimum energy structure for $(HNO_3)\cdot(NO_2)$ is planar and the orientation of the O–H bond of HNO_3 is toward an oxygen atom of NO_2 (Fig. 1a). Bond angle and distance criteria[57,58] indicate that a hydrogen bond exists between O(3)–H···O(6). Similar results were obtained using the ROHF and B3LYP methods. The ZPE-corrected binding energies for $(HNO_3)\cdot(NO_2)$ are between −2.4 and −2.8 kcal mol^{-1}, depending upon the method (Table 1). These are weak compared to the binding energies reported for the nitric acid–water complex which are in the range of 7–10 kcal mol^{-1}.[23,59,60] Assuming similar entropy changes upon complex formation, the enthalpy differences result in the equilibrium constant for complex formation with H_2O being larger than that for complex formation with NO_2 by at least a factor of 10^2 at 300 K.

Table 1 Binding energies of the complexes before (D_0) and after (D_e) the zero-point energy correction

	ROHF/TZP		ROMP2/TZP		B3LYP/TZP	
Complex	D_0/kcal mol^{-1}	D_e/kcal mol^{-1}	D_0/kcal mol^{-1}	D_e/kcal mol^{-1}	D_0/kcal mol^{-1}	D_e/kcal mol^{-1}
$(HNO_3)\cdot(NO_2)$	−3.7	−2.8	−3.3	−2.4	−3.3	−2.5
$(NO_3^-)\cdot(NO_2)$	−4.6	−3.9	−3.9	−3.1	−6.0	−5.5
$(HNO_3)\cdot(N_2O_4)$	−7.8	−7.0	−8.2	−7.3	−6.0	−5.5
$(NO_3^-)\cdot(N_2O_4)$	−14.0	−13.1	−13.1	−12.2	−14.6	−14.0

The structure is nearly identical to the B3LYP/6-31G(d,p) structure for $(HNO_3)\cdot(NO_2)$ reported by Dimitrova and Peyerimhoff,[61] who reported an MP2/6-311+G** binding energy for $(HNO_3)\cdot(NO_2)$ of −4.4 kcal mol^{-1}, without correcting for ZPE.

$(HNO_3)\cdot(N_2O_4)$

The ROMP2 optimized structure for $(HNO_3)\cdot(N_2O_4)$ is shown in Fig. 1b. Similar to $(HNO_3)\cdot(NO_2)$, the O–H bond of HNO_3 is oriented towards the two O atoms of N_2O_4 in the complex and is involved in hydrogen bonding. The four remaining atoms of N_2O_4 tilt away from the HNO_3 subunit. The internal coordinates of HNO_3 and N_2O_4 are not substantially distorted by complexation. The ROMP2 structure of $(HNO_3)\cdot(N_2O_4)$ is very similar to the corresponding ROHF and B3LYP structures, although the N–N bond length in the N_2O_4 subunit is approximately 0.20 Å shorter than in the ROMP2 and B3LYP structures. A similar difference is observed in the N–N bond length of isolated N_2O_4 using ROHF *versus* the other two methods. We suggest that this may be due to the incorrect assignment of local molecular orbital energies because of the absence of correlation in the ROHF Hamiltonian.

Table 1 shows that the calculated binding energies for $(HNO_3)\cdot(N_2O_4)$ are more than twice as large as corresponding binding energies for $(HNO_3)\cdot(NO_2)$. While there is one hydrogen bond in the $(HNO_3)\cdot(N_2O_4)$, the stronger binding energy relative to $(HNO_3)\cdot(NO_2)$ arises from the strong dipole-induced dipole interaction between N_2O_4 and HNO_3 in the complex. The experimental polarizability of N_2O_4 is double that of NO_2[62–64] and is more susceptible to charge distortion near polar molecules like HNO_3. The Löwdin charges calculated here also confirm that N_2O_4 is polarized by HNO_3 in the complex through a dipole-induced dipole effect.

$(NO_3^-)\cdot(NO_2)$

Fig. 1c shows the ROMP2 optimized structure of $(NO_3^-)\cdot(NO_2)$. The ROMP2, ROHF and B3LYP structures for this complex are very similar. In general, nitrogen atoms of NO_3^- and NO_2 are separated in the complex by a relatively short distance, 3.27–3.38 Å, depending upon the method. The NO_3^- subunit remains planar in the complex. The N–O bond lengths of NO_3· remain nearly equivalent to one another in $(NO_3^-)\cdot(NO_2)$. The sums of the atomic charges for NO_3^- and NO_2 in the complex were always near −1.0 and 0.0, respectively, suggesting that NO_3^- remains a closed-shell anion when complexed to NO_2. Table 1 shows the ZPE-corrected binding energies for $(NO_3^-)\cdot(NO_2)$ which are larger than those obtained for $(HNO_3)\cdot(NO_2)$ by all three methods.

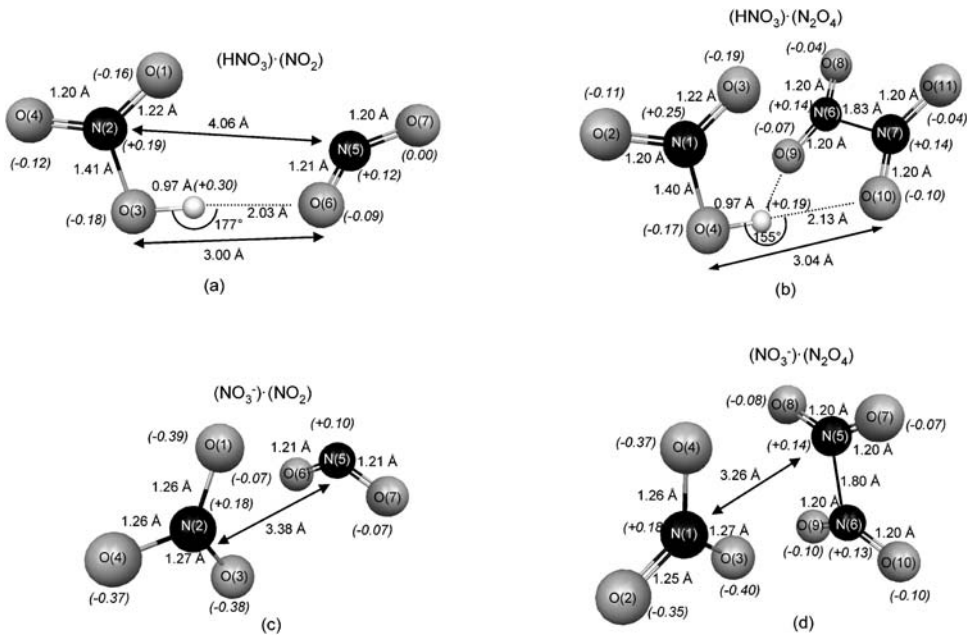

Fig. 1 The ROMP2/TZP optimized structures of (a) $(HNO_3)\cdot(NO_2)$, (b) $(HNO_3)\cdot(N_2O_4)$, (c) $(NO_3^-)\cdot(NO_2)$, and (d) $(NO_3^-)\cdot(N_2O_4)$. Löwdin atomic charges are listed adjacent to the atoms in parentheses.

$(NO_3^-)\cdot(N_2O_4)$

The ROMP2-optimized structure of $(NO_3^-)\cdot(N_2O_4)$ is shown in Fig. 1d. Calculations indicate that the binding of NO_3^- to N_2O_4 is a very exoergic process with computed binding energies that are about twice as large as those calculated for the next most stable complex, $(HNO_3)\cdot(N_2O_4)$; Table 1. The strong interaction is attributed to an ion-induced dipole effect. The large polarizability of N_2O_4 relative to NO_2 makes N_2O_4 more susceptible to induction *via* the electric field of NO_3^-, causing the N_2O_4 subunit to be polarized along the axis of the N–N bond.

Calculated vibrational frequencies of the NO_x complexes

Detecting NO_x complexes based on their Raman shifts or infrared absorption bands is complicated due to interferences between vibrational features of the complexes and the subunits making up the complexes. Infrared absorption intensities, Raman activities, vibrational frequencies, and vibrational frequency shifts due to complexation for the four complexes were calculated to aid in identifying these complexes in laboratory experiments. Emphasis is placed on identifying the vibrational modes of the complexes whose frequencies are shifted from their corresponding values in the uncomplexed molecules. The calculated and experimentally determined frequencies of the uncomplexed molecules are tabulated in the ESI† and will not be discussed in detail here since a number of high level modeling studies have been reported for the molecular vibrations of N_2O_4,[28,65–72] HNO_3,[45,64,73–75] and NO_2.[76,77]

The calculated spectroscopic results for $(HNO_3)\cdot(NO_2)$ are given in Table 2. Rows corresponding to modes that may be identified by infrared and/or Raman spectroscopy are highlighted in boldface and italics, respectively. The last six modes listed for $(HNO_3)\cdot(NO_2)$ are intermolecular modes whose atomic motions tend to involve atoms on both subunits. Modes 1–12 correspond to vibrations that are intramolecular modes involving atoms on only one subunit.

Mode 1 of $(HNO_3)\cdot(NO_2)$ corresponds to O–H stretching in the HNO_3 subunit. It has a computed band at 3714 cm^{-1} that is shifted −70 cm^{-1} and is ~5 times stronger than the corresponding band calculated for isolated HNO_3. The utility of this mode in experimental studies will most likely depend upon the presence of water which has vibrational frequencies near 3400 cm^{-1}.[78] Other potentially useful vibrational modes include the Raman-active ONO bend in the NO_2 subunit (mode 8) and mode 12 corresponding to HONO torsion in the HNO_3 subunit, which should be detectable with IR spectroscopy.

Dimitrova[79] used several theoretical methods along with a scaling procedure to calculate predicted experimental frequencies and frequency shifts for $(HNO_3)\cdot(NO_2)$. The average percent deviation between our ROMP2/TZP predicted experimental frequencies and those computed by Dimitrova's best method (B3LYP/6-31G(d,p)) was 3.6%. For vibrational modes in which our ROMP2/TZP and Dimitrova's B3LYP/6-31G(d,p) calculations both predict non-zero frequency shifts, the direction of the shift is the same in nine out of ten cases.

Finally, Barnes *et al.*[32] have reported the infrared spectrum of $(HNO_3)\cdot(NO_2)$ in an argon matrix. They assigned two bands to the O–H stretching and HONO torsion vibrations of HNO_3 and one band to the asymmetric stretching mode of NO_2. Our ROMP2/TZP predicted experimental frequencies for these three modes are in good agreement with the measured peak frequencies of Barnes, deviating by an average of only 3.3%. Dimitrova's B3LYP/6-31G(d,p) predicted frequencies were also in good agreement with Barnes' frequencies, deviating by an average of 3.8%.

The vibrational frequencies for $(HNO_3)\cdot(N_2O_4)$ are presented in Table 3. Mode 6 of $(HNO_3)\cdot(N_2O_4)$ is due to HON bending in the HNO_3 subunit and is a good candidate for identification

Table 2 Vibrational frequencies, infrared intensities, and Raman intensities for $(HNO_3)\cdot(NO_2)$ obtained using ROMP2/TZP

$(HNO_3)\cdot(NO_2)$		Frequencies			Calculated intensities	
Mode	Description	Calculated/cm^{-1}	Shift[a]/cm^{-1}	Predicted[a] experimental/cm^{-1}	Infrared/km mol^{-1}	Raman/$Å^4$ amu^{-1}
1	***OH stretch of HNO_3***	***3714***	***−70***	***3422***	***440***	***49***
2	ONO asymmetric stretch of HNO_3	1853	−11	1687	190	20
3	ONO asymmetric stretch of NO_2	1844	0	1618	400	240
4	**HON bend of HNO_3**	**1395**	**+44**	**1390**	**99**	**7.1**
5	ONO asymmetric stretch of NO_2	1340	+18	1336	6.1	740
6	ONO asymmetric stretch of HNO_3	1319	+5	1317	240	17
7	(H)ON stretch of HNO_3	912	+17	920	210	12
8	*ONO bend of NO_2*	*802*	*+29*	*779*	*18*	*720*
9	OOON torsion of HNO_3	765	+5	773	4.1	0.8
10	ONO bend of HNO_3	677	+16	680	130	7.6
11	(H)ONO bend of HNO_3	609	+17	615	7.9	4.6
12	**HONO torsion of HNO_3**	**599**	**+140**	**619**	**110**	**1.4**
13	Intermolecular	114	N.A.	114	5.0	1.0
14	Intermolecular	98	N.A.	98	0.68	2.5
15	Intermolecular	83	N.A.	83	1.1	1.8
16	Intermolecular	57	N.A.	57	0.81	4.4
17	Intermolecular	27	N.A.	27	0.41	1.6
18	Intermolecular	26	N.A.	26	0.83	1.5

[a] A scaling procedure was used to obtain more accurate calculated vibrational frequencies for the modes of the complexes. To do this, a frequency shift for each mode was obtained. The frequency shift is the difference between the computed frequency of the mode in the complex and the computed frequency of the corresponding mode in the isolated subunit. The shift is then added to the experimental derived frequency of the corresponding mode (taken from the literature) to generate a predicted experimental frequency for the vibrational mode in the complex.

Table 3 Vibrational frequencies, infrared intensities, and Raman intensities for $(HNO_3)\cdot(N_2O_4)$ obtained using ROMP2/TZP

$(HNO_3)\cdot(N_2O_4)$		Frequencies			Calculated intensities	
Mode	Description	Calculated/ cm^{-1}	Shift[a]/ cm^{-1}	Predicted[a] experimental/ cm^{-1}	Infrared/ km mol^{-1}	Raman/ $Å^4$ amu^{-1}
1	***OH stretch of HNO_3***	***3719***	***−65***	***3427***	***280***	***83***
2	In phase ONO asymmetric stretch of N_2O_4	1957	**+10**	**1728**	280	5.0
3	180° Out of phase ONO asymmetric stretch of N_2O_4	1916	−1	1717	50	34
4	ONO asymmetric stretch of HNO_3	1844	−20	1678	350	11
5	In phase ONO asymmetric stretch of N_2O_4	1409	+4	1387	5.4	12
6	**HON bend of HNO_3**	**1401**	**+50**	**1396**	**81**	**4.6**
7	ONO symmetric stretch of HNO_3	1322	+8	1320	210	28
8	180° Out of phase symmetric stretch of N_2O_4	1274	+4	1265	410	0.67
9	(H)ON stretch of HNO_3	921	+26	929	170	8.0
10	In phase ONO bend of N_2O_4	833	+4	817	1.7	14
11	OOON torsion of HNO_3	767	+7	775	2.5	0.12
12	180° Out of phase ONO bend of N_2O_4	761	+11	762	280	0.11
13	ONO bend of HNO_3	682	+21	685	9.4	5.3
14	NOON torsion of N_2O_4	642	+5	662	0.050	0.40
15	(H)ONO bend of HNO_3	613	+21	619	5.5	4.6
16	**HONO torsion of HNO_3**	**508**	**+49**	**528**	**26**	**0.70**
17	In phase ONN bend of N_2O_4	478	+8	488	0.51	20
18	OOON torsion of N_2O_4	405	+5	430	9.7	0.2
19	NN stretch of N_2O_4	266	+9	271	0.021	37
20	OON bend of N_2O_4	214	+12	277	0.38	1.7
21	Intermolecular	124	N.A.	124	0.15	0.4
22	Intermolecular	121	N.A.	121	3.1	0.9
23	Intermolecular	100	N.A.	100	2.4	2.1
24	ONNO torsion of N_2O_4	72	−20	62	0.099	0.7
25	Intermolecular	56	N.A.	56	0.069	1.7
26	Intermolecular	41	N.A.	41	0.99	3.7
27	Intermolecular	24	N.A.	24	1.0	6.1

[a] For explanation of how shift and predicted experimental frequency were calculated see Table 2 footnote.

using IR, although it may be obscured by the asymmetric NO_2 stretch of the NO_3^- ion at 1356 cm^{-1}, which tends to be very broad.[80] Mode 1 of $(HNO_3)\cdot(N_2O_4)$, corresponding to the O–H stretch of the HNO_3 subunit, should be detectable by both IR and Raman spectroscopy at 3427 cm^{-1}, although the presence of water could preclude its detection. The increased intensity and red shift clearly indicates hydrogen bonding.[58]

Vibrational data for $(NO_3^-)\cdot(NO_2)$ are presented in Table 4. This complex does not possess unique vibrational modes that could be used to identify it on surfaces. However, modes 2 and 3 of $(NO_3^-)\cdot(NO_2)$, which correspond to degenerate asymmetric stretching in the NO_3^- subunit, could be suitable markers for measuring $(NO_3^-)\cdot(NO_2)$ in a molecular beam experiment where peaks are narrower.

Data for $(NO_3^-)\cdot(N_2O_4)$ are presented in Table 5. Mode 15, which is due to the OOON torsion in the N_2O_4 subunit, and the in-phase symmetric stretch in the N_2O_4 subunit (mode 5), may be useful to detect $(NO_3^-)\cdot(N_2O_4)$ using IR spectroscopy.

Table 4 Vibrational frequencies, infrared intensities, and Raman intensities for $(NO_3)\cdot(NO_2)$ obtained using ROMP2/TZP

$(NO_3^-)\cdot(NO_2)$		Frequencies			Calculated intensities	
Mode	Description	Calculated/cm^{-1}	Shift[a]/cm^{-1}	Predicted[a] experimental/cm^{-1}	Infrared/km mol^{-1}	Raman/$Å^4$ amu^{-1}
1	ONO asymmetric stretch of NO_2	1855	+11	1629	240	20
2	NO_3^- asymmetric stretch of NO_3^-	1510	+17	1373	630	12
3	NO_3^- asymmetric stretch of NO_3^-	1477	−16	1340	570	5.2
4	ONO symmetric stretch of NO_2	1335	+13	1331	4.1	1.4
5	*NO_3^- symmetric stretch of NO_3^-*	*1067*	*+1*	1051	*0.43*	*47*
6	OOON torsion of NO_3^-	830	−3	828	8.0	0.1
7	ONO bend of NO_2	773	+1	751	2.6	1.4
8	ONO bend of NO_3^-	728	+2	722	14	5.3
9	ONO bend of NO_3^-	728	+2	722	0.65	4.2
10	Intermolecular	159	N.A.	159	6.3	4.5
11	Intermolecular	101	N.A.	101	0.43	7.8
12	Intermolecular	84	N.A.	84	7.7	0.2
13	Intermolecular	68	N.A.	68	1.4	0.1
14	Intermolecular	50	N.A.	50	0.042	3.5
15	Intermolecular	16	N.A.	16	0.19	0.3

[a] For explanation of how shift and predicted experimental frequency were calculated see Table 2 footnote.

Table 5 Vibrational frequencies, infrared intensities, and Raman intensities for $(NO_3^-)\cdot(N_2O_4)$ obtained using ROMP2/TZP

$(NO_3^-)\cdot(N_2O_4)$		Frequencies			Calculated intensities	
Mode	Description	Calculated/ cm^{-1}	Shift/ cm^{-1}	Predicted experimental/ cm^{-1}	Infrared/km mol^{-1}	Raman/Å^4 amu^{-1}
1	In phase ONO asymmetric stretch of N_2O_4	1962	+15	1776	260	3.1
2	180° out of phase ONO asymmetric stretch of N_2O_4	1906	−11	1707	78	17
3	**Asymmetric stretch of NO_3^-**	**1536**	**+43**	**1399**	**590**	**4.3**
4	**Asymmetric stretch of NO_3^-**	**1462**	**−31**	**1325**	**630**	**4.2**
5	**In phase ONO symmetric stretch of N_2O_4**	**1408**	**+3**	**1389**	**35**	**13**
6	180° out of phase symmetric stretch of N_2O_4	1280	+10	1271	300	1.5
7	Symmetric stretch of NO_3^-	1072	+6	1072[a]	3.7	11
8	In phase ONO bend of N_2O_4	836	+7	820	3.0	25
9	OOON torsion of NO_3^-	828	−1	828[a]	8.3	0.32
10	180° out of phase ONO bend of N_2O_4	763	+13	764	200	1.1
11	ONO bend of NO_3^-	731	+5	731[a]	3.4	16
12	ONO bend of NO_3^-	728	+2	728[a]	4.2	33
13	NOON torsion of N_2O_4	637	**0**	**657**	0.57	6.7
14	In phase ONN bend of N_2O_4	496	+26	506	0.13	5.5
15	**OOON torsion of N_2O_4**	**443**	**+43**	**468**	**31**	**2.6**
16	NN stretch of N_2O_4	277	+20	282	1.2	26
17	ONN bend of N_2O_4	227	+25	290	0.0055	0.21
18	**Intermolecular**	**131**	**N.A.**	**131**	**14**	**0.73**
19	ONNO torsion of N_2O_4	125	**+33**	**115**	0.59	0.39
20	Intermolecular	102	N.A.	102	1.1	5.0
21	Intermolecular	84	N.A.	84	1.4	3.4
22	Intermolecular	63	N.A.	63	0.42	9.5
23	Intermolecular	37	N.A.	37	0/011	2.1
24	Intermolecular	14	N.A.	14	0.31	6.7

[a] For explanation of how shift and predicted experimental frequency were calculated see Table 2 footnote.

Electronic spectroscopy of N_2O_4 complexes

Electronic transitions of $(HNO_3)\cdot(N_2O_4)$, $(NO_3^-)\cdot(N_2O_4)$, and N_2O_4 were explored using configuration interaction singles (CIS) to identify to what extent the complexes absorb visible radiation. If they absorb visible light strongly then the photoactivation of these complexes *via* solar radiation might lead to chemistry that generates HONO or other volatile nitrogen oxides on urban surfaces.

When the CIS method was applied to isolated N_2O_4, the computed energy difference between the ground and first excited electronic states of the molecule was computed to be 4.38 eV (283 nm). The experimental gas-phase spectrum of N_2O_4 has a strong absorption band centered at 340 nm (3.65 eV). Therefore, the CIS approach overestimates the energy for the transition in isolated N_2O_4 by 0.73 eV.[31,53] Based on this we corrected the calculated CIS transition energies for $(HNO_3)\cdot(N_2O_4)$, $(NO_3^-)\cdot(N_2O_4)$ by 0.73 eV.

That is,

$$\Delta E_{(corr)} = \Delta E_{(CIS)} - 0.73\ eV \qquad (6)$$

where $\Delta E_{(corr)}$ and $\Delta E_{(CIS)}$ are the corrected and uncorrected vertical excitation energies of the complexes, respectively.

The CIS results for isolated N_2O_4 indicate that the transition between the ground and first excited state involves the promotion of an electron from a σ-bonding HOMO to a π-bonding LUMO, both located along the N–N axis of the molecule, in agreement with the DFT results Chesnut *et al.*[81] For $(HNO_3)\cdot(N_2O_4)$ and $(NO_3^-)\cdot(N_2O_4)$, the CIS results indicate that the orbitals involved in the ground to first excited electronic state transition were very similar to those in isolated N_2O_4, supporting the application of the energy correction described above. The corrected vertical excitation energy from the ground electronic state to the first excited electronic state of $(HNO_3)\cdot(N_2O_4)$ is $\Delta E_{(corr)} = 3.69$ eV, or 336 nm. The intensity for the transition was nearly three times as strong as in isolated N_2O_4 at $f = 1.7 \times 10^{-4}$ [σ_A(336 nm) = 1.8×10^{-18} cm^2, base 10]. The $\Delta E_{(corr)}$ for $(NO_3^-)\cdot(N_2O_4)$ is 3.90 eV (318 nm), with an intensity of $f = 9.3 \times 10^{-4}$ [σ_A (318 nm) = 9.9×10^{-18} cm^2, base 10], more than an order of magnitude larger than in isolated N_2O_4. In both complexes, excitation involves the promotion of an electron from a σ-bonding orbital to the LUMO π-bonding orbital. In the case of $(NO_3^-)\cdot(N_2O_4)$, the σ orbital, which is not the HOMO, also has significant density on the NO_3^- subunit and therefore excitation to the π-orbital may destabilize the complex. These results indicate that $(HNO_3)\cdot(N_2O_4)$ and $(NO_3^-)\cdot(N_2O_4)$ are strong absorbers of light in the region above the 290 nm actinic cutoff,[1] indicating they may play an important role in initiating photochemistry that generates HONO or other volatile nitrogen species on surfaces.

H-Atom transfer in $(HNO_3)\cdot(N_2O_4)$

A potential intramolecular hydrogen atom transfer reaction within the $(HNO_3)\cdot(N_2O_4)$ complexes to form HONO was investigated by performing a series of constrained optimizations at multiple points along a plausible chemical reaction pathway using ROMP2/TZP, which was less problematic with regard to orbital convergence than B3LYP/TZP.

The postulated mechanism for H-atom transfer in $(HNO_3)\cdot(N_2O_4)$ consisted of two steps and leads to the formation of a $(HONO)\cdot(N_2O_5)$ complex (Fig. 2). Step 1 consists of moving the H-atom of HNO_3 incrementally from the HNO_3 subunit

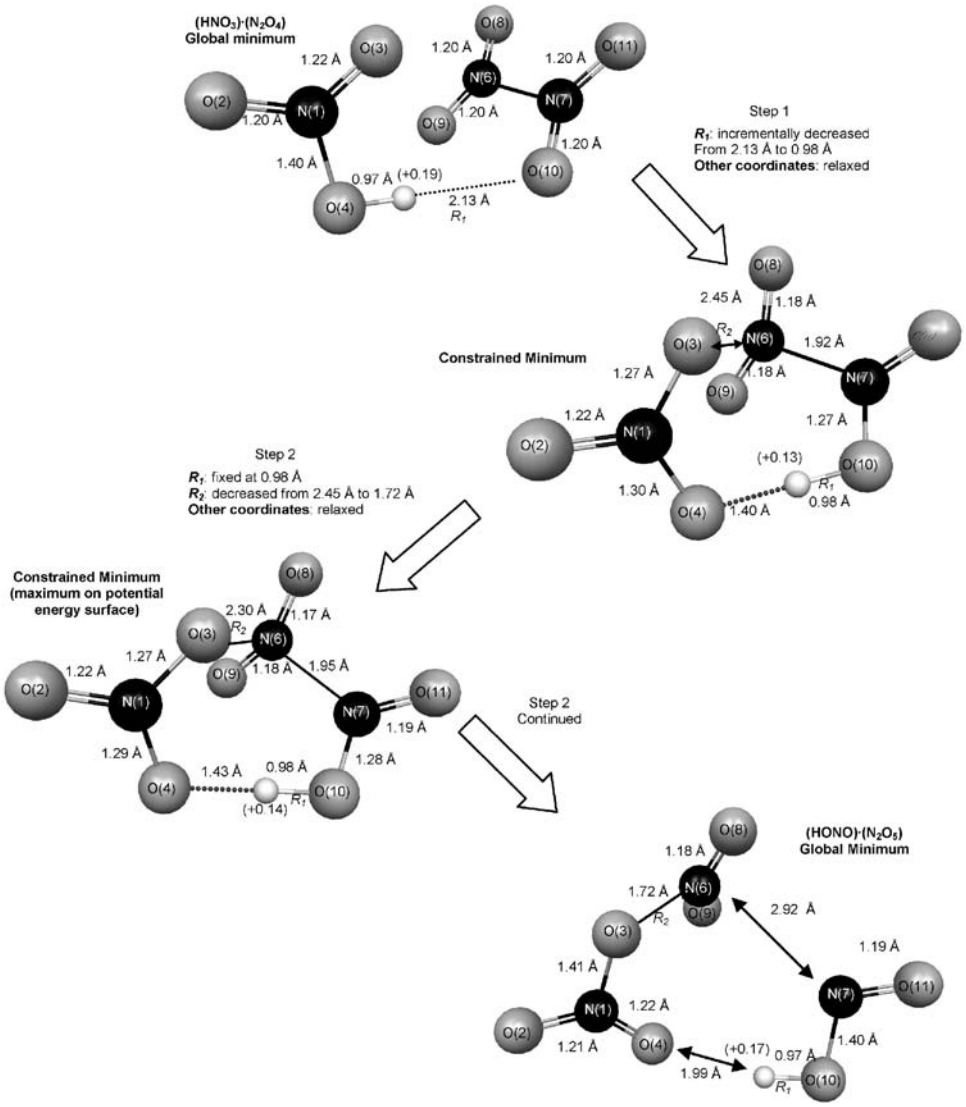

Fig. 2 Computed pathway for H-atom transfer within $(HNO_3)\cdot(N_2O_4)$ to form $(HONO)\cdot(N_2O_5)$.

toward O(10) of N_2O_4 until a HONO moiety is formed. At this point the H–O distance in the HONO moiety is 0.98 Å, identical to the ROMP2/TZP value for isolated *trans*-HONO. A constrained optimization was then performed at each increment by fixing the O(10)···H distance R_1 and allowing all other coordinates to optimize. The potential energy of each partially optimized structure is plotted as a function of R_1 in Fig. 3a, and shows that the energy necessary to move the H-atom across the interior of the complex to N_2O_4, forming *trans*-HONO, is 41 kcal mol^{-1}.

Step 2 proceeds by gradually decreasing the N(6)···O(3) distance R_2 from 2.45 to 1.72 Å, forming an N_2O_5-like structure complexed to *trans*-HONO. A plot of the potential energy as a function of R_2 (Fig. 3b) reveals a maximum of 34.5 kcal mol^{-1} at R_2 = 2.3 Å, with a structure corresponding $(HONO)\cdot(N_2O_5)$. As R_2 increases the calculated bond order of the N(6)–N(7) bond decreases until it is less than 0.05 in the final structure of step 2. The H-atom charges for all structures depicted in Fig. 2 are between +0.19 and +0.17, suggesting this reaction is truly a hydrogen atom transfer reaction and not a proton transfer reaction.

The energy barrier associated with the H-atom transfer within $(HNO_3)\cdot(N_2O_4)$ to form $(HONO)\cdot(N_2O_5)$ was computed to be 40.9 kcal mol^{-1}, corresponding to an excitation threshold of 702 nm. This estimate should be considered an upper limit for the true energy barrier of the reaction. The energy of the product complex was computed to be 17.4 kcal mol^{-1} less than that of the maximum energy structure in Step 2, indicating the reaction is thermally irreversible; the barrier is too large to be overcome thermally or through a vibrational overtone excitation of the HNO_3 O–H bond. However, a photochemical mechanism due to the absorption of solar radiation is possible. The $(HONO)\cdot(N_2O_5)$ formed has a moderate ROMP2 ZPE-corrected binding energy of −4.8 kcal mol^{-1}, indicating that it is weakly stable and may dissociate to form volatile *trans*-HONO. It is likely that H_2O present on a surface will compete with N_2O_5 for the HONO produced since the binding energy for the $(HONO)\cdot(H_2O)$ complex is very similar at −5.3 kcal mol^{-1}.[23] The ΔE for the overall

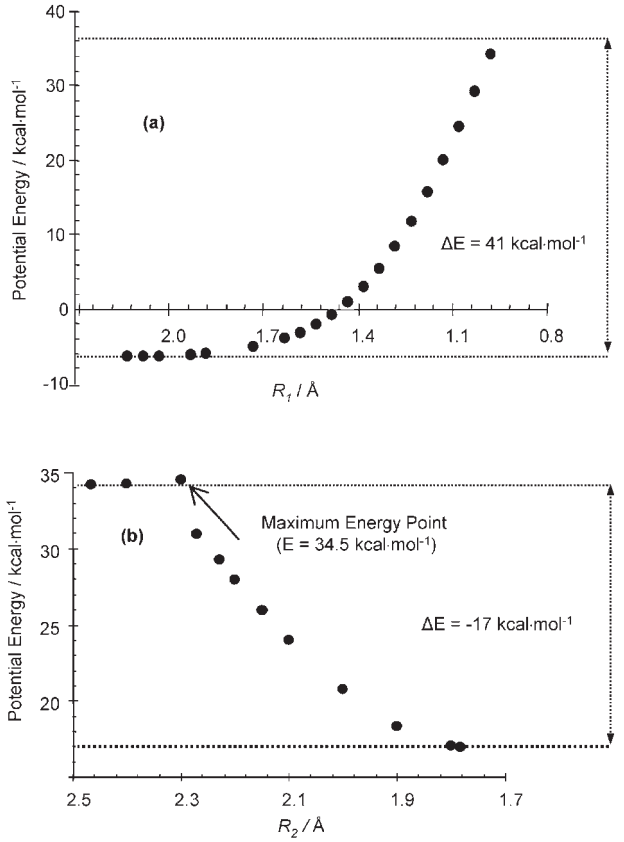

Fig. 3 Energetics of the H-atom transfer mechanism in the $(HNO_3)\cdot(N_2O_4)$ complex depicted in Fig. 2 showing potential energy *versus*: (a) R_1 for step 1, and (b) R_2 for step 2.

reaction $HNO_3 + N_2O_4 \rightarrow$ *trans*-HONO $+ N_2O_5$ was computed to be 22 kcal mol^{-1}, in fair agreement with the experimental 298 K enthalpy ΔH of 14 kcal mol^{-1} calculated using the NIST-JANAF Thermochemical Tables.[82]

H-Atom transfer in $(HNO_3)\cdot(NO_2)$

H-Atom abstraction within the $(HNO_3)\cdot(NO_2)$ complex was treated as a 3-step process (Fig. 4). In Step 1, the O(7) atom was rotated toward the HNO_3 subunit by adjusting the torsion angle τ defined by O(7), N(5), O(6), and O(3) from its equilibrium value of 164° to 0°. At $\tau = 0°$ O(7) points directly towards HNO_3 and its partial negative charge is expected to reduce the energy required to transfer the H-atom. The potential energy values for the partially optimized structures (all internal coordinates optimized except for τ) are displayed as a function of τ in Fig. 5a and show that the energy required to rotate O(7) towards HNO_3 is only 0.41 kcal mol^{-1}.

In Step 2 the distance R_1 between the H-atom of HNO_3 and O(6) of the NO_2 subunit was incrementally decreased from 2.07 Å to the equilibrium O–H bond length of 0.97 Å in the ROMP2/TZP optimized HONO. A plot of potential energy as a function of R_1 (Fig. 5b) shows that transfer of the H-atom between the two subunits of the complex is accompanied by a rise in potential energy until a maximum is reached at 49.7 kcal mol^{-1}.

In Step 3, the NO_3 subunit of the complex was gradually forced away from the H-atom. The internal coordinate R_2, which is the distance between the H-atom and the N of the NO_3 subunit was incrementally adjusted from 2.09 to 3.05 Å while R_2 and R_1 were fixed during the optimizations to prevent relaxation back to the reactants. The other internal coordinates were optimized. The potential energy of the system decreased with increasing R_2 as shown in Fig. 5c. A full optimization was then performed on the $R_2 = 3.05$ Å structure to generate a local minimum for $(HONO)\cdot(NO_3)$ with an energy of 46.2 kcal mol^{-1}. Interestingly, the charge of the H-atom varies from +0.30 in $(HNO_3)\cdot(NO_2)$ to a high of +0.37 in a transitional structure, and decreases to +0.23 in $(HONO)\cdot(NO_3)$; Fig. 4. This indicates that the reaction can be thought of as part way between a proton transfer and H-atom transfer reaction.

Two other stable configurations of $(HONO)\cdot(NO_3)$ were located, having energies 42.1 kcal mol^{-1} and 43.1 kcal mol^{-1} greater than the combined energy of isolated HNO_3 and NO_2 (see the ESI†). All three $(HONO)\cdot(NO_3)$ complexes are weakly bound and should dissociate to produce surface HONO and NO_3. The HONO generated may immediately bind to HNO_3, the ROMP2/TZP ZPE-corrected binding energy of $(HONO)\cdot(HNO_3)$ is −3.5 kcal mol^{-1}, only slightly stronger than $(HONO)\cdot(NO_3)$. Therefore, we anticipate that surface water will displace HONO from the surface-bound $(HONO)\cdot(HNO_3)$ complex leading to volatilization of HONO. Alternatively, HONO may form a complex with H_2O on surfaces. The ZPE-corrected binding energy for the $(HONO)\cdot(H_2O)$ complex was reported to be −5.3 kcal mol^{-1}.[23]

The energy barrier for the H-atom abstraction/proton transfer within $(HNO_3)\cdot(NO_2)$ to form $(HONO)\cdot(NO_3)$ is computed to be 52.2 kcal mol^{-1}. This corresponds to visible light with a wavelength of 548 nm. The potential energy of the product complex was computed to be just 3.5 kcal mol^{-1} lower than the potential energy of the maximum energy structure, indicating that the reaction is reversible. However, the ΔE for the overall reaction $HNO_3 + NO_2 \rightarrow$ *trans*-HONO $+ NO_3$ was computed to be 46 kcal mol^{-1}.

While this is significantly greater than the enthalpy of 24 kcal mol^{-1} calculated from the NIST-JANAF thermochemical tables,[82] it is still likely that HONO can be formed from H-atom transfer within the $(HNO_3)\cdot(NO_2)$ complex *via* photoexcitation.

ATR-FTIR investigation of HNO_3–NO_x surface films

A series of ATR-FTIR experiments were carried out to search for complexes of HNO_3 with NO_2 or N_2O_4 on the surface of a SiO_x-coated AMTIR internal reflection element (IRE). Initially the IRE was exposed to 2.3 Torr of anhydrous HNO_3. While this is a much larger concentration than found in the atmosphere, searching for the very existence of these complexes requires higher concentrations to obtain detectable signals. Fig. 6a shows bands due to surface-adsorbed HNO_3 at 1671 and 1303 cm^{-1} assigned to the ONO-asymmetric stretch (ν_{as}) and mixed modes of the ONO-symmetric stretch (ν_s) and NOH bend (δ), respectively. The broad feature at 1394 cm^{-1} is the ν_{3a} (antisymmetric NO_2 stretch) of nitrate, present in small quantities on the surface.[83] Additional bands due to O–H stretches of $HNO_3\cdot(H_2O)_n$ (n = 1–3) complexes were also observed in the present study between 2400 and 3200 cm^{-1} (not shown), similar to what was observed previously.[22] The presence of nitrate and nitric acid–water complexes

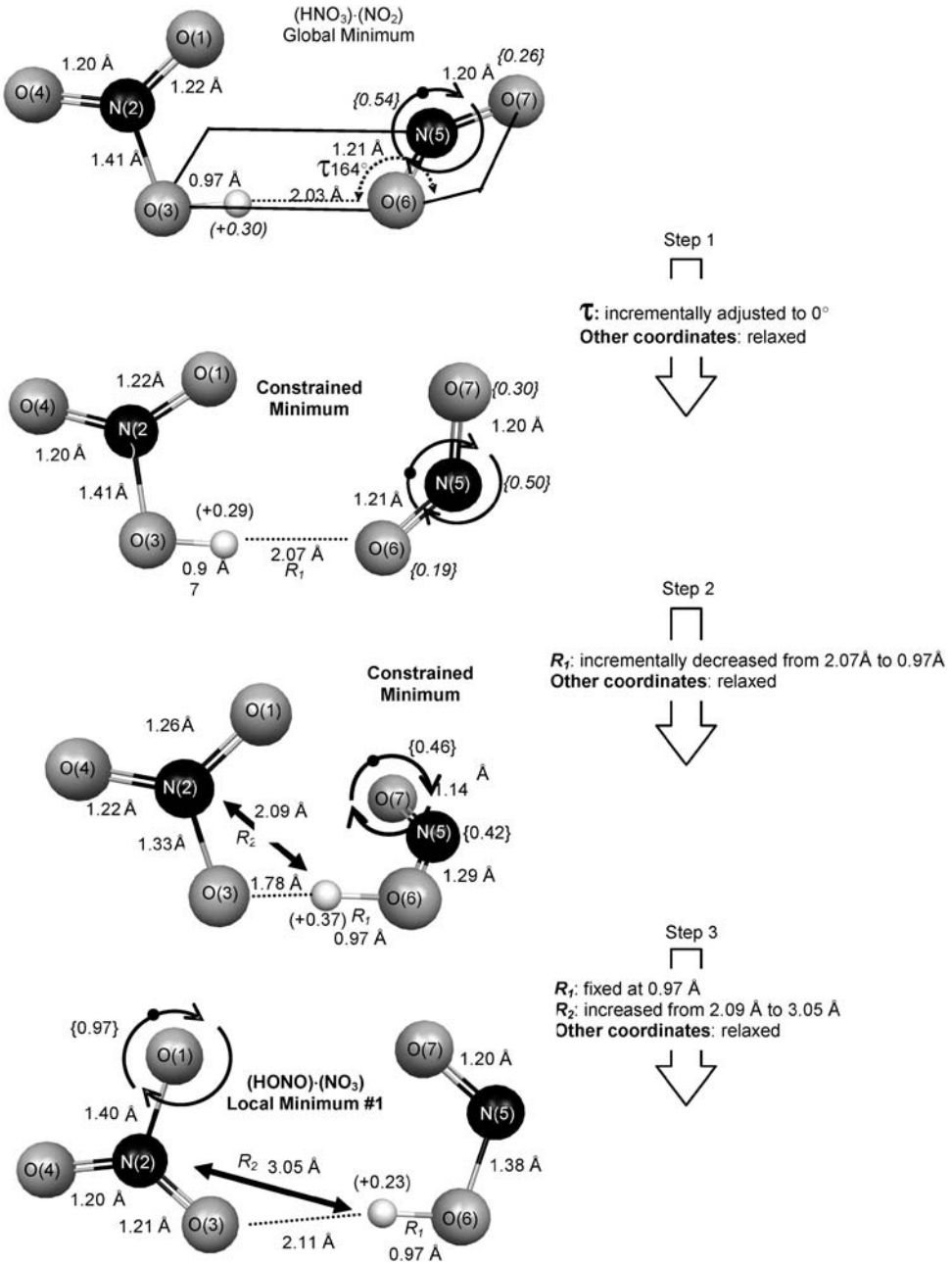

Fig. 4 Computed pathway for H-atom transfer within $(HNO_3)\cdot(NO_2)$ to form $(HONO)\cdot(NO_3)$.

suggests that residual water remains on the surface of the IRE, despite efforts to remove it under vacuum.

An infrared spectrum of species adsorbed to the surface of SiO_x-coated AMTIR during exposure to 2.3 Torr anhydrous HNO_3 and 58 Torr of NO_2–N_2O_4 is shown in Fig. 6b for the region 800–1800 cm^{-1}. The spectrum was obtained by taking the ratio of the single beam spectrum in the presence of a mixture of HNO_3–NO_2–N_2O_4 to that of anhydrous HNO_3 shown in Fig. 6a. Absorption bands attributed to HNO_3 are present at 1667 and 1303 cm^{-1}. Strong bands at 1743 and 1256 cm^{-1} are related to surface-adsorbed N_2O_4, as confirmed by comparison to a reference spectrum obtained by exposing a clean SiO_x-AMTIR surface to 84 Torr of NO_2–N_2O_4 (Fig. 6c). As discussed below, these are assigned to N_2O_4 complexed to HNO_3 and NO_3^-. The reference spectrum of NO_2–N_2O_4 has weak features in the region 1300–1700 cm^{-1} that coincide with peaks shown in Fig. 6b. These arise from the reaction of N_2O_4 with residual water on the SiO_x-coated AMTIR surface to form nitric acid complexes.

New bands at 1632 and 1602 cm^{-1} appear in the spectrum obtained when the IRE is exposed to an HNO_3–NO_2–N_2O_4 mixture. These peaks disappeared when the reaction chamber was evacuated, suggesting that species responsible for these peaks are not held on the surface by strong interactions. The band at 1632 cm^{-1} in Fig. 6b is attributed to the $\nu_{as}(NO_2)$ of NO_2 complexed to NO_3^-, in agreement with the *ab initio*

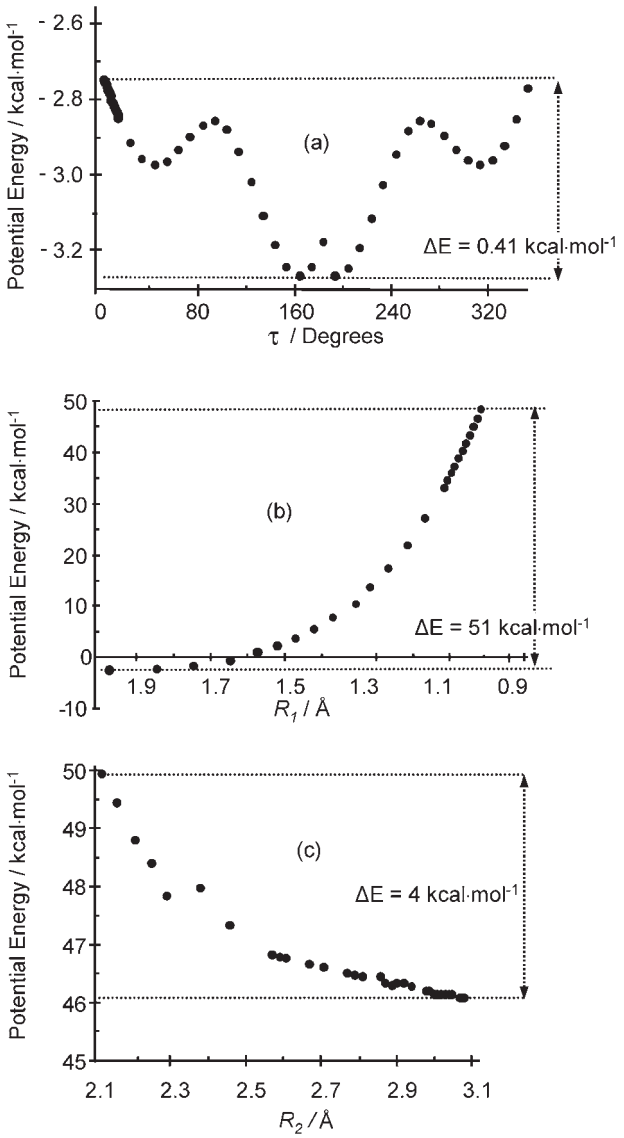

Fig. 5 Energetics of the H-atom transfer in the $(HNO_3)\cdot(NO_2)$ complex depicted in Fig. 4 showing potential energy *versus*: (a) τ for step 1, (b) R_1 for step 2, and (c) R_2 for step 3.

calculations that predict a $+11$ cm^{-1} shift in this mode relative to free NO_2 (Table 4). The band at 1602 cm^{-1} is assigned to the $\nu_{as}(NO_2)$ of nitrogen dioxide in the $(HNO_3)\cdot(NO_2)$ complex. This is based on the ROMP2/TZP infrared frequencies that predict an insignificant shift for the $\nu_{as}(NO_2)$ mode of $(HNO_3)\cdot(NO_2)$ relative to free NO_2, and the lack of detectable amounts of NO_2 on surfaces in the absence of HNO_3. In recent experiments using ATR-FTIR to study the hydrolysis of NO_2 on surfaces, Ramazan *et al.*[22] observed a peak at 1600 cm^{-1} under conditions closer to those found in a polluted atmosphere. In their study of $(HNO_3)\cdot(NO_2)$ in a frozen argon matrix, Barnes *et al.*[32] reported a band centered at 1606 cm^{-1}, shifted by just -5 cm^{-1} with respect to the ν_{as} band of NO_2 observed in the absence of HNO_3. Barnes *et al.*[32] also reported bands at 3441 and 561 cm^{-1} and attributed them to the O–H stretch and NOH torsion of the $(HNO_3)\cdot(NO_2)$ complex. A band at 3441 cm^{-1} was absent from our spectra of the HNO_3–NO_2–N_2O_4 mixture,

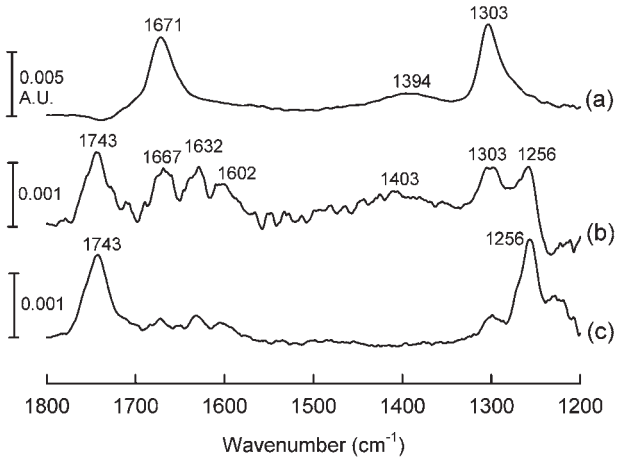

Fig. 6 Spectrum of SiO_x-coated AMTIR crystal exposed to (a) 2.3 Torr anhydrous HNO_3 only; (b) 2.3 Torr anhydrous HNO_3 and 46 Torr of NO_2–N_2O_4; (c) 84 Torr of NO_2–N_2O_4 only.

but this is not surprising since this is expected to be very broad under the conditions of the experiment. The NOH torsion lies outside the spectral range of the IRE and detector used.

We assign the bands at 1743 and 1256 cm^{-1} to $\nu_s(NO_2)$ and $\nu_{as}(NO_2)$ of N_2O_4 complexed to HNO_3 and NO_3^-. The peaks in Fig. 6b are indistinguishable from N_2O_4 on the surface in the absence of added HNO_3 or NO_3^-. However, calculations predict shifts of $+15$ cm^{-1} at the most for $\nu_{as}(NO_2)$ stretches of N_2O_4 upon complexation with HNO_3 and such differences will not be easily distinguishable due to the broad peaks in these experiments. The fact that N_2O_4 is observed on the surface in Fig. 6b and c and that enhanced levels of N_2O_4 have been observed on surfaces containing nitric acid in other systems[20,21,27] suggests that N_2O_4 forms complexes with HNO_3 or NO_3^- on surfaces.

This is supported by calculated equilibrium constants for $(HNO_3)\cdot(NO_2)$ and $(HNO_3)\cdot(N_2O_4)$, which are 0.007 atm^{-1} and 0.25 atm^{-1} at 298 K, respectively. Under the present conditions, this would correspond to a concentration of $(HNO_3)\cdot(N_2O_4)$ that is $\sim$15 times higher than $(HNO_3)\cdot(NO_2)$. Although all calculations here are for the gas-phase rather than for complexes on surfaces, the trend is consistent with the observations shown in Fig. 6c where the area of the peak at 1743 cm^{-1} is approximately double that of the peak at 1602 cm^{-1}. As seen in Fig. 6c, even trace amounts of water will lead to HNO_3 formation in the presence of N_2O_4 and subsequent formation of nitric acid–nitrate complexes will lead to enhanced uptake of N_2O_4 on the surface. We also considered the possibility that N_2O_4 is complexed to SiOH on the IRE surface.[84] Complexes of HNO_3 and N_2O_4 with free OH groups on the IRE surface are formed during initial exposure to N_2O_4, as indicated by a reduction of free SiOH stretch at 3650–3800 cm^{-1}. However, the surface quickly saturates and the ν(SiO–H) peak intensity remains constant, while peaks attributed to N_2O_4 continue to increase in intensity linearly with NO_2/N_2O_4 concentration due to further complexation to HNO_3 and NO_3^-.

UV/visible spectrum of N_2O_4 in aqueous nitric acid

Fig. 7 shows the UV/vis absorption spectra of N_2O_4 dissolved in concentrated HNO_3 and in acetonitrile, respectively. For

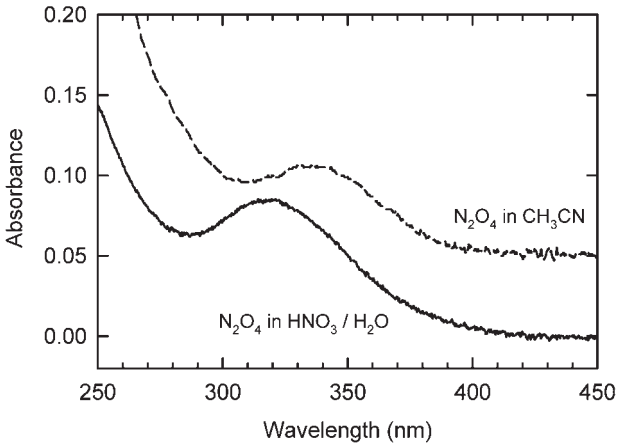

Fig. 7 UV/vis absorption spectra of (a) N_2O_4 dissolved in a solution of 70% w/w HNO_3–H_2O (solid line) and (b) N_2O_4 dissolved in anhydrous acetonitrile (spectrum shifted along *y*-axis for clarity). The spectrum in N_2O_4 in HNO_3 was obtained by subtracting from the spectrum of a solution of HNO_3–H_2O from a spectrum of HNO_3–H_2O–N_2O_4.

solutions of N_2O_4 in HNO_3–H_2O, a distinct band is observed centered at 320 nm with a tail that extends out to 340 nm. In the N_2O_4–acetonitrile spectrum, there is an absorbance band centered at 338 nm, similar to what is observed for N_2O_4 dissolved in hexane (λ_{max} = 343 nm)[85] and methylene chloride ($\lambda_{max} \approx$ 340 nm).[86] The band center locations in the UV/vis spectra of N_2O_4 in acetonitrile, hexane, and methylene chloride are very similar to the band center location in the spectrum of gaseous N_2O_4.[30] This is expected since there is a lack of strong solute–solvent interactions in these mixtures. The approximately 20 nm blue shift in the absorbance band of N_2O_4 in concentrated nitric acid relative to N_2O_4 in organic solvents having minimal solvent–solute interactions is in excellent agreement with the −22 nm shift in the vertical excitation energies of $(NO_3^-)\cdot(N_2O_4)$ relative to isolated N_2O_4 derived from CIS calculations. It was not possible to determine the molar absorption coefficients for the HNO_3–N_2O_4 solution since the pathlength between the quartz coverslips used to contain the solutions was indeterminate. Solutions in cuvettes with longer and defined pathlengths absorbed too strongly at wavelengths less than 340 nm to resolve the N_2O_4 absorption band.

Formation of the $(NO_3^-)\cdot(N_2O_4)$ complex in concentrated HNO_3 requires the presence of NO_3^-. While undissociated HNO_3 is favored in concentrated solutions of HNO_3, spectroscopic studies have shown NO_3^- is present in such solutions, due in part to the ionization of N_2O_4.[87,88] The UV/vis absorption spectra presented here support the existence of the $(NO_3^-)\cdot(N_2O_4)$ complex and is consistent with the enhancement of visible light absorption for solutions of N_2O_4 and HNO_3.

Atmospheric implications

HNO_3 and NO_3^- are ubiquitous components of urban surface films,[89] resulting from heterogeneous chemistry such as NO_2 and N_2O_5 hydrolysis, and deposition of HNO_3 and nitrate-containing particles.[1] HNO_3 and NO_3^- are considered "end products" of atmospheric oxidation of gaseous nitrogen oxides emitted during fossil fuel combustion. Consequently, NO_x will be present near boundary layer surfaces that hold the acid and the anion, creating conditions favorable for forming the type of complexes investigated here.

The calculations show that complexes of N_2O_4 with HNO_3 and NO_3^- are more stable than those with NO_2, and hence more likely to play a role in heterogeneous chemistry at room temperature. One argument against a significant role for N_2O_4 is that the concentrations in equilibrium with atmospherically relevant concentrations of NO_2 are quite small, since the equilibrium constant[90] for the $2NO_2 \leftrightarrow N_2O_4$ reaction is only 2.8×10^{-19} cm^3 molecule^{-1}. For example, at 100 ppb NO_2, the concentration of N_2O_4 in equilibrium with it is only 0.07 ppt in the gas phase. However, the gas-phase equilibrium does not accurately represent condensed phase N_2O_4 concentrations. Experimental evidence[87,91] suggests that N_2O_4 is the dominant species formed in solution, with solution phase equilibrium constants 3–4 orders of magnitude higher than the gas-phase equilibrium.[92] The stability of the N_2O_4 complexes with HNO_3 and NO_3^- predicted here suggests that the surface concentration of N_2O_4 may also be larger than expected from the gas phase equilibrium.[21] The amount of the surface-bound dimer may be limited by the amount of available adsorbed HNO_3 and NO_3^-. Therefore, one may expect surfaces to hold increasing amounts of N_2O_4 in the form of the complexes as more complexing species are generated in such reactions as (1) and the hydrolysis of N_2O_5.

Some of these complexes may play a key role in the thermal reaction (1). For example, the source of the surface N_2O_4 could be a sequential complexation of NO_2 to HNO_3 to form $(HNO_3)\cdot(NO_2)$ and then $(HNO_3)\cdot(O_2NNO_2)$ or $(HNO_3)\cdot(ONONO_2)$. In any event, if there is an equilibrium concentration of $(HNO_3)\cdot(NO_2)$ complexes on the surface and the rate determining step for forming $(HNO_3)\cdot(ONONO_2)$ and then HONO + HNO_3 is uptake of NO_2 from the gas phase, the formation of HONO would be first order in gas phase NO_2, consistent with experimental observations.[5,27,93–100] It is also possible that the $(HNO_3)\cdot(N_2O_4)$ will be only short-lived and spontaneously undergo ionization to $NO^+NO_3^-$, followed by protonation to yield HONO and HNO_3. The present studies also show that the photochemically driven transfer of a hydrogen atom from HNO_3 to NO_2 and N_2O_4 to form HONO are feasible.

The calculations presented here show that N_2O_4 does indeed lend its photochemical properties to the complexes with HNO_3 and NO_3^-. The peak of the transition to the first excited state for N_2O_4 alone is centered at 340 nm, but the absorption band is broad and extends beyond 430 nm.[101] This suggests that light absorption by the $(HNO_3)\cdot(N_2O_4)$ and $(NO_3^-)\cdot(N_2O_4)$ complexes, which are predicted to occur at 336 and 318 nm, respectively, will also extend out into the visible region. The N–N bond energy of N_2O_4 is 12.7 kcal mol^{-1},[102] much less than the excitation energy of the chromophore. Therefore, the adsorption of a photon by the $(HNO_3)\cdot(N_2O_4)$ complex may result in fragmentation of N_2O_4 into electronically excited NO_2* and a ground state NO_2, similar to what is observed in the photodissociation of free N_2O_4.[103] The electronically excited NO_2* generated during this process may react with water or HNO_3 on the surface, analogous to what was proposed by Li *et al.* in the gas phase.[33]

It is intriguing that irradiation of humidified air in the SAPHIR chamber produced HONO at a rate of 0.391 ppb h^{-1} with the 370 nm cutoff filter in place and 0.665 ppb h^{-1} for the experiment without the filter.[26] This is only a factor of 1.7 decrease in the HONO production rate, and should be much larger if HNO_3, NO_3^-, or N_2O_4 were the precursors. This and the fact that HONO production could be parameterized based on NO_2 photolysis is consistent with surface $(HNO_3)\cdot(NO_2)$ or $(NO_3^-)\cdot(NO_2)$ being the photolytic HONO precursor. In the case of $(NO_3^-)\cdot(NO_2)$, electronically excited NO_2 would abstract a proton from water or nitric acid co-adsorbed on the surface. While the photochemical evidence favors this explanation, the weak gas-phase binding energy of especially $(HNO_3)\cdot(NO_2)$ would seem to preclude it from being the HONO source in the SAPHIR experiments. Conversely, the complexes $(HNO_3)\cdot(N_2O_4)$ and $(NO_3^-)\cdot(N_2O_4)$ that have substantial binding energies to hold NO_x to surfaces, absorb light at $\lambda < 370$ nm and do not explain the HONO production rates in the cutoff filter experiments. However, it should be emphasized that the binding energies calculated here are for gas-phase species and the interactions between NO_2 and HNO_3 and NO_3 may be very different in surface films comprised of complex mixtures.

The present calculations did not include water which is present on all surfaces in the lower atmosphere. Infrared spectroscopic studies show that at 50% relative humidity during the NO_2 heterogeneous hydrolysis, the major hydrate of HNO_3 on the surface is the monohydrate.[22] The binding energy of HNO_3 to one water molecule in the gas phase is calculated to be $\sim$8 kcal mol^{-1},[23,104,105] similar to the binding energy of 7 kcal mol^{-1} for HNO_3 to N_2O_4 calculated here (Table 1). The role of water is more complex than simply binding to surface species, however, since it also assists in the isomerization[106] of symmetric to asymmetric N_2O_4 and reacts with the autoionized $NO^+NO_3^-$ to form HONO and HNO_3 on the surface.

Furthermore, water has been shown to displace HONO from surfaces into the gas phase in both laboratory and field studies.[107,108] Whether this is a simple competitive adsorption/desorption process or a chemical reaction with a HONO precursor is not known. However, if a complex such as $(HNO_3)\cdot(N_2O_4)$ is a precursor to HONO, the latter may be initially bound to HNO_3 when it is formed on the surface. The release of HONO upon the addition of water vapor or increase in the relative humidity may be due to stronger binding of H_2O to HNO_3 than of HONO to HNO_3, thus causing HONO to be displaced. We have computed the ROMP2 binding energy of the $(HNO_3)\cdot(HONO)$ complex. The ZPE corrected binding energy of this complex is -3.5 kcal mol^{-1} and is small compared with the binding energy for $(HNO_3)\cdot(H_2O)$ complex, which is about -7 to -10 kcal mol^{-1}.[59,60]

In summary, the calculations presented here highlight the potential importance of HNO_3 and NO_3^- complexes with oxides of nitrogen on surfaces. Such complexes may be key intermediates in the thermal and photochemical production of HONO in the absence of organic compounds.

Acknowledgements

We are grateful to the National Science Foundation for support of this work through the Environmental Molecular Sciences Institute (grant number 0431512). We thank Prof. Mark Bachmann and his group at the UCI Integrated Nanosystems Research Facility for providing plasma-enhanced chemical vapor deposition capabilities. L.F.P. thanks the Erskine Fund of the University of Canterbury for assistance with travel expenses. We also thank Dr Sotiris Xantheas at Pacific Northwest National Laboratory for helpful discussions and comments on the manuscript.

References

1 B. J. Finlayson-Pitts and J. N. Pitts, Jr, *Chemistry of the Upper and Lower Atmosphere—Theory, Experiments, and Applications*, Academic Press, San Diego, 2000.
2 A. M. Winer and H. W. Biermann, *Res. Chem. Intermed.*, 1994, **20**, 423–445.
3 B. Alicke, U. Platt and J. Stutz, *J. Geophys. Res., [Atmos.]*, 2002, **107**, , DOI: 10.1029/2000JD000075.
4 J. Stutz, B. Alicke and A. Neftel, *J. Geophys. Res., [Atmos.]*, 2002, **107**, , DOI: 10.1029/2001JD000390.
5 J. Kleffmann, K. H. Becker and P. Wiesen, *Atmos. Environ.*, 1998, **32**, 2721–2729.
6 J. Kleffmann, T. Gavriloaiei, A. Hofzumahaus, F. Holland, R. Koppmann, L. Rupp, E. Schlosser, M. Siese and A. Wahner, *Geophys. Res. Lett.*, 2005, **32**, L05818.
7 X. Zhou, H. J. Beine, R. E. Honrath, J. D. Fuentes, W. Simpson, P. B. Shepson and J. W. Bottenheim, *Geophys. Res. Lett.*, 2001, **28**, 4087–4090.
8 X. Zhou, K. Civerolo, H. Dai, G. Huang, J. Schwab and K. Demerjian, *J. Geophys. Res., [Atmos.]*, 2002, **107**.
9 H. Akimoto, H. Takagi and F. Sakamaki, *Int. J. Chem. Kinet.*, 1987, **19**, 539–551.
10 X. Zhou, H. Gao, Y. He, G. Huang, S. B. Bertman, K. Civerolo and J. Schwab, *Geophys. Res. Lett.*, 2003, **30**, , DOI: 10.1029/2003GL018620.
11 K. A. Ramazan, D. Syomin and B. J. Finlayson-Pitts, *Phys. Chem. Chem. Phys.*, 2004, **6**, 3836–3843.
12 C. George, R. S. Strekowski, J. Kleffmann, K. Stemmler and M. Ammann, *Faraday Discuss.*, 2005, **130**, 195–210.
13 I. Bejan, Y. Abd El Aal, I. Barnes, T. Benter, B. Bohn, P. Wiesen and J. Kleffmann, *Phys. Chem. Chem. Phys.*, 2006, **8**, 2028–2035.
14 K. Stemmler, M. Ammann, C. Donders, J. Kleffmann and C. George, *Nature*, 2006, **440**, 195–198.
15 X. Zhou, Y. Hi, G. Huang, T. D. Thornberry, M. A. Carroll and S. B. Bertman, *Geophys. Res. Lett.*, 2002, **29**, , DOI: 10.1029/2002GL015080.
16 F. Rohrer, B. Bohn, T. Brauers, D. Bruning, F. J. Johnen, A. Wahner and J. Kleffmann, *Atmos. Chem. Phys.*, 2005, **5**, 2189–2201.
17 W. P. L. Carter, R. Atkinson, A. M. Winer and J. N. J. Pitts, *Int. J. Chem. Kinet.*, 1981, **13**, 735–740.
18 W. P. L. Carter, R. Atkinson, A. M. Winer and J. N. J. Pitts, *Int. J. Chem. Kinet.*, 1982, **14**, 1071–1103.
19 W. P. L. Carter, R. Atkinson, A. M. Winer and J. N. Pitts, *Atmos. Environ.*, 1985, **19**, 1977–1978.
20 A. L. Goodman, G. M. Underwood and V. H. Grassian, *J. Phys. Chem. A*, 1999, **103**, 7217–7223.
21 W. S. Barney and B. J. Finlayson-Pitts, *J. Phys. Chem. A*, 2000, **104**, 171–175.
22 K. A. Ramazan, L. M. Wingen, Y. Miller, G. M. Chaban, R. B. Gerber, S. S. Xantheas and B. J. Finlayson-Pitts, *J. Phys. Chem. A*, 2006, **110**, 6886–6897.
23 M. Staikova and D. J. Donaldson, *Phys. Chem. Chem. Phys.*, 2001, **3**, 1999–2006.
24 J. Mack and J. R. Bolton, *J. Photochem. Photobiol., A*, 1999, **128**, 1–13.
25 H. Herrmann, *Phys. Chem. Chem. Phys.*, 2007, **9**, 3935–3964.
26 F. Rohrer, B. Bohn, T. Brauers, D. Bruning, F. J. Johnen, A. Wahner and J. Kleffmann, *Atmos. Chem. Phys.*, 2005, **5**, 2189–2201.
27 B. J. Finlayson-Pitts, L. M. Wingen, A. L. Sumner, D. Syomin and K. A. Ramazan, *Phys. Chem. Chem. Phys.*, 2003, **5**, 223–242.
28 A. S. Pimentel, F. C. A. Lima and A. B. F. da Silva, *J. Phys. Chem. A*, 2007, **111**, 2913–2920.

29 A. S. Pimentel, F. C. A. Lima and A. B. F. da Silva, *Chem. Phys. Lett*., 2007, **436**, 47–50.
30 M. H. Harwood and R. L. Jones, *J. Geophys. Res., [Atmos.]*, 1994, **99**, 22955–22964.
31 T. C. Hall and F. E. Blacet, *J. Chem. Phys*., 1952, **20**, 1745–1749.
32 A. J. Barnes, E. Lasson and C. J. Nielsen, *J. Mol. Struct*., 1994, **322**, 165–174.
33 S. Li, J. Matthews and A. Sinha, *Science*, 2008, **21**, 1657–1660.
34 J. N. Crowley and S. A. Carl, *23*, 1997, **101**, 4178–4184.
35 P. O. Wennberg and D. Dabdub, *Science*, 2008, **319**, 1624–1625.
36 T. Berces and S. Forgeteg, *Trans. Faraday Soc*., 1970, **66**, 640–647.
37 S. Jaffe and H. W. Ford, *J. Phys. Chem*., 1967, **71**, 1832–1835.
38 H. S. Johnston, S. G. Chang and G. Whitten, *J. Phys. Chem*., 1974, **78**, 1–7.
39 C. C. J. Roothaan, *Rev. Mod. Phys*., 1960, **32**, 179–185.
40 C. Lee, W. Yang and R. G. Parr, *Phys. Rev. B*, 1988, **37**, 785–789.
41 A. D. Becke, *Phys. Rev. A*, 1988, **38**, 3098–3110.
42 A. D. Becke, *J. Chem. Phys*., 1992, **96**, 2155–2160.
43 C. Moeller and M. S. Plesset, *Phys. Rev*., 1934, **46**, 618–622.
44 T. H. Dunning, *J. Chem. Phys*., 1971, **55**, 716–723.
45 Y. Miller, G. M. Chaban and R. B. Gerber, *Chem. Phys*., 2005, **313**, 213–224.
46 P. O. Lowdin, *Adv. Quantum Chem*., 1970, **5**, 185–189.
47 R. C. Hilborn, *Am. J. Phys*., 1982, **50**, 982–986.
48 J. B. Foresman, M. Head-Gordon, J. A. Pople and M. J. Frish, *J. Phys. Chem*., 1992, **96**, 135–149.
49 P. G. Jasien and L. L. Weber, *THEOCHEM*, 2001, **572**, 203–212.
50 J. Abe and Y. Shirai, *J. Am. Chem. Soc*., 1996, **118**, 4705–4706.
51 D. T. Major and B. Fischer, *J. Phys. Chem. A*, 2003, **107**, 8923–8931.
52 W. Bartkowiak and P. Lipkowski, *J. Mol. Model*., 2005, **11**, 317–322.
53 A. M. Bass, A. E. L., Jr and A. H. Laufer, *J. Res. Natl. Bur. Stand. Sect. A*, 1976, **80**, 143–166.
54 M. S. Gordon and M. W. Schmidt, in *Theory and Applications of Computational Chemistry: the First Forty Years*, ed. C. E. Dykstra, G. Frenking, K. S. Kim and G. E. Scuseria, Elsevier, Amsterdam, 2005, pp. 1167–1189.
55 M. W. Schmidt, K. K. Baldridge, J. A. Boatz, S. T. Elbert, M. S. Gordon, J. H. Jensen, S. Koseki, N. Matsunaga, K. A. Nguyen, S. Su, T. L. Windus, M. Dupuis and J. A. Montgomery, *J. Comput. Chem*., 1993, **14**, 1347–1363.
56 A. Komornicki and J. W. McIver, *J. Chem. Phys*., 1979, **70**, 2014–2016.
57 Z. Rahim and B. N. Barman, *Acta Crystallogr., Sect. A*, 1978, **34**, 761–764.
58 S. Scheiner, *Annu. Rev. Phys. Chem*., 1994, **45**, 23–56.
59 J. R. Scott and J. B. Wright, *J. Phys. Chem. A*, 2004, **108**, 10578–10585.
60 F.-M. Tao, K. Higgins, W. Klemperer and D. D. Nelson, *Geophys. Res. Lett*., 1996, **23**, 1797–1800.
61 Y. Dimitrova and S. Peyerimhoff, *Chem. Phys.*, 2000, **254**, 125–134.
62 D. Goebel, U. Hohm, K. Kerl, U. Trumper and G. Maroulis, *J. Phys. Chem*., 1994, **98**, 13123–13130.
63 W. A. Guillory and M. L. Bernstein, *J. Chem. Phys*., 1975, **62**, 1058–1060.
64 P. R. McCurdy, W. P. Hess and S. S. Xantheas, *J. Phys. Chem. A*, 2002, **106**, 7628–7635.
65 Y. Elyoussofi, M. Herman, J. Lievin and I. Kleiner, *Spectrochim. Acta, Part A*, 1997, **53**, 881–894.
66 T. Kato, M. Oobatake, K. Machida and S. Hayashi, *Mol. Phys*., 1992, **77**, 177–192.
67 S. S. Wesolowski, J. T. Fermann, T. D. Crawford and H. F. S. II, *J. Chem. Phys*., 1997, **106**, 7178–7184.
68 E. L. Varetti and G. C. Pimentel, *J. Chem. Phys*., 1971, **55**, 3813.
69 F. Bolduan and H. J. Jodl, *Chem. Phys. Lett*., 1982, **85** 283–286.
70 D. E. Tevault and L. Andrews, *Spectrochim. Acta, Part A*, 1974, **30**, 969.
71 C. H. Bibart and G. E. Ewing, *J. Chem. Phys*., 1974, **61**, 1284–1292.
72 D. Luckhaus and M. Quack, *Chem. Phys. Lett*., 1992, **199**, 293–301.
73 Y. Dimitrova, *Spectrochim. Acta, Part A*, 2004, **60**, 1–8.
74 K. J. Feierabend, D. K. Havey, M. E. Varner, J. F. Stanton and V. Vaida, *J. Chem. Phys*., 2006, **124**, 124323.
75 H. G. Kjaergaard, *J. Phys. Chem. A*, 2002, **106**, 2979–2987.
76 K. Uzi, *Chem. Phys. Lett*., 1990, **170**, 17–20.
77 T. Schimanouchi, *Tables of Molecular Vibrational Frequencies, Part 5*, NSRDS-NBS 39, 1972.
78 S. Y. Venyaminov and F. G. Prendergast, *Anal. Biochem*., 1997, **248**, 234–245.
79 Y. Dimitrova, *Spectrochim. Acta, PartA*, 2003, **59**, 1919–1927.
80 D. Forney, W. E. Thompson and M. E. Jacox, *J. Chem. Phys*., 1993, **99**, 7393.
81 D. B. Chesnut and A. L. Crumbliss, *Chem. Phys*., 2005, **315**, 53–58.
82 M. W. Chase, *NIST-JANAF Thermochemical Tables*, American Chemical Society, American Institute of Physics for the National Institute of Standards and Technology, Washington, DC, 1998.
83 D. Sporleder and G. E. Ewing, *J. Phys. Chem. A*, 2001, **105**, 1838–1846.
84 K. C. Thompson and P. Margey, *Phys. Chem. Chem. Phys*., 2003, **5**, 2970–2975.
85 K. Y. Lee, C. Amatore and J. K. Kochi, *J. Phys. Chem*., 1991, **95**, 1285–1294.
86 E. Bosch and J. K. Kochi, *J. Org. Chem*., 1994, **59**, 3314–3325.
87 D. J. Millen and D. Watson, *J. Chem. Soc*., 1957, 1369–1372.
88 J. E. Harrar, L. P. Rigdon and S. F. Rice, *J. Raman Spectrosc*., 1997, **28**, 891–899.
89 B. Lam, M. L. Diamond, A. J. Simpson, P. A. Makar, J. Truong and N. A. Hernandez-Martinez, *Atmos. Environ*., 2005, **35**, 6578–6586.
90 S. P. Sander, A. R. Ravishankara, R. R. Friedl, D. M. Golden, C. E. Kolb, M. J. Kurylo, M. J. Molina, G. K. Moortgat, B. J. Finlayson-Pitts, P. H. Wine, R. E. Huie and V. L. Orkin, *Chemical Kinetics and Photochemical Data for Use in Atmospheric Studies. Evaluation Number 15 JPL Publication 06-2*, National Aeronautics and Space Administration, Jet Propulsion Laboratory, Pasadena, CA, 2006.
91 C. C. Addison, *Chem. Rev*., 1980, **80**, 21–39.
92 T. F. Redmond and B. B. Wayland, *J. Phys. Chem*., 1968, **72**, 1626–1629.
93 J. N. Pitts, E. Sanhueza, R. Atkinson, W. P. L. Carter, A. M. Winer, G. W. Harris and C. N. Plum, *Int. J. Chem. Kinet*., 1984, **16**, 919–939.
94 J. N. Pitts, Jr, T. J. Wallington, H. W. Biermann and A. M. Winer, *Atmos. Environ*., 1985, **19**, 763–767.
95 A. Febo and C. Perrino, *Atmos. Environ., Part A*, 1991, **25**, 1055–1061.
96 F. Sakamaki, S. Hatakeyama and H. Akimoto, *Int. J. Chem. Kinet*., 1983, **15**, 1013–1029.
97 R. Svensson, E. Ljungstrom and O. Lindqvist, *Atmos. Environ*., 1987, **21**, 1529–1539.
98 M. E. Jenkin, R. A. Cox and D. J. Williams, *Atmos. Environ*., 1988, **22**, 487–498.
99 P. Wiesen, J. Kleffmann, R. Kurtenbach and K. H. Becker, *Faraday Discuss*., 1995, **100**, 121–127.
100 R. M. Harrison and G. M. Collins, *J. Atmos. Chem*., 1998, **30**, 397–406.
101 M. H. Harwood and R. L. Jones, *J. Geophys. Res., [Atmos.]*, 1994, **99**, 22955–22964.
102 I. C. Hisatsune, *J. Phys. Chem*., 1961, **65**, 2249–2253.
103 G. Inoue, Y. Nakata, Y. Usui, H. Akimoto and M. Okuda, *J. Chem. Phys*., 1979, **70**, 3689–3693.
104 R. Atkinson, D. L. Baulch, R. A. Cox, J. N. Crowley, R. F. Hampson, R. G. Hynes, M. E. Jenkins, M. J. Rossi and J. Troe, *Atmos. Chem. Phys*., 2004, **4**, 1461–1738.
105 F. M. Tao, K. Higgins, W. Klemperer and D. D. Nelson, *Geophys. Res. Lett*., 1996, **23**, 1797–1800.
106 A. S. Pimentel, F. C. A. Lima and A. B. F. d. Silva, *J. Phys. Chem. A*, 2007, **111**, 2913–2920.
107 D. A. Syomin and B. J. Finlayson-Pitts, *Phys. Chem. Chem. Phys*., 2003, **5**, 5236–5242.
108 J. Stutz, B. Alicke, R. Ackermann, A. Geyer, S. H. Wang, A. B. White, E. J. Williams, C. W. Spicer and J. D. Fast, *J. Geophys. Res., [Atmos.]*, 2004, **109**.

